



# Identifying the oxygen evolution mechanism by microkinetic modelling of cyclic voltammograms

Janis Geppert<sup>a,b</sup>, Fabian Kubannek<sup>b</sup>, Philipp Röse<sup>a</sup>, Ulrike Krewer<sup>a,\*</sup>

<sup>a</sup>Institute for Applied Materials - Electrochemical Technologies, Karlsruhe Institute of Technology, Adenauerring 20b, Karlsruhe, Germany

<sup>b</sup>Institute of Energy and Process Systems Engineering, Technische Universität Braunschweig, Franz-Liszt-Str. 35, Braunschweig, Germany



## ARTICLE INFO

### Article history:

Received 14 December 2020

Revised 13 January 2021

Accepted 30 January 2021

Available online 3 February 2021

### Keywords:

Hydrous iridium

Oxygen evolution reaction

Mechanistic study

Reaction kinetics

Surface coverage

Electrocatalytic watersplitting

Dynamic simulation

## ABSTRACT

Electrocatalytic water splitting is currently one of the most promising reactions to produce “green” hydrogen in a decarbonized energy system. Its bottleneck reaction, the oxygen evolution reaction (OER), is catalysed by hydrous iridium, a stable and active catalyst material. Improving the OER requires a better and especially quantitative understanding of the reaction mechanism as well as its kinetics. In this work, we present an experimentally validated microkinetic model that allows to quantify the mechanistic pathways, emerging surface species prior and during the OER, the reaction rates for the single steps and essential thermodynamic properties. Therefore, two mechanisms based on density functional theory and experimental findings are evaluated on which only simulation results of the theory-based one are found to be in full accordance with cyclic voltammograms even at different potential rates and, thus, able to describe the catalytic system. The simulation implies that oxygen is evolving mostly via a fast single site pathway ( $*OO \rightarrow * + O_2$ ) with an effective reaction rate, which is several orders of magnitude faster compared to the slow dual site ( $2^*O \rightarrow 2^* + O_2$ ) pathway rate. Intermediate states of roughly 7% Ir(III), 25% Ir(IV) and 63% Ir(V) are present at typical OER potentials of 1.6 V vs RHE. We are able to explain counterintuitive experimental findings of a reduced iridium species during highly oxidizing potentials by the kinetic limitation of water adsorption. Although water adsorption is in general thermodynamically favourable, it is kinetically proceeding slower than the electrochemical steps at high potential. In the lower potential range from 0.05 to 1.5 V vs RHE the stepwise oxidation of the iridium is accompanied with van der Waals like ad- and desorption processes, which leads in comparison to Langmuir-type adsorption to a broadened peak shape in the cyclic voltammograms. Overall, our analysis shows that the dynamic microkinetic modelling approach is a powerful tool to analyse catalytic microkinetics in depth and to bridge the gap between thermodynamic calculations and experiments.

© 2021 The Authors. Published by Elsevier Ltd.

This is an open access article under the CC BY license (<http://creativecommons.org/licenses/by/4.0/>)

## 1. Introduction

On the quest for a sustainable energy supply based on renewable technologies, such as wind and solar energy, efficient conversion and storage strategies are needed [1]. A key technology is the electrocatalytic splitting of water into hydrogen and oxygen. While the hydrogen evolution reaction can be performed smoothly by platinum based catalysts, the mayor challenge is to understand and develop active and stable catalyst materials to reduce the high overpotential of its counterpart, the oxygen evolution reac-

tion (OER). In acidic environment, anodically grown hydrous iridium is revealed as highly active and has been widely studied concerning its electrochemical characteristics [2–4]. The stability during the OER seems promising: hydrous Ir [5] but also metallic Ir [6] and the oxide IrO<sub>2</sub> [7] exhibit lower dissolution rates compared to their highly active competitors based on Ru [7]. In direct comparison, metallic Ir is more active but less stable than IrO<sub>2</sub>. Hydrous Ir is even more active, since also sites in the near surface structure catalyse the OER [8]. Knowledge of the microkinetics of a reaction allows to identify slow and fast steps and to deduce possible improvements. To study the microkinetics, a valid mechanism assumption based on good understanding of the surface changes is needed. The present understanding of processes during OER is briefly summarised in the following paragraph.

During the OER, electrocatalytically active catalysts are known to form adsorbed hydroxide and oxygen at its catalyst-electrolyte

\* Corresponding author at: Institute for Applied Materials – Electrochemical Technologies, Karlsruhe Institute of Technology, Adenauerring 20b, Karlsruhe, Germany.

E-mail addresses: [janis.geppert@kit.edu](mailto:janis.geppert@kit.edu) (J. Geppert),

[f.kubannek@tu-braunschweig.de](mailto:f.kubannek@tu-braunschweig.de) (F. Kubannek), [philipp.roese@kit.edu](mailto:philipp.roese@kit.edu) (P. Röse), [ulrike.krewer@kit.edu](mailto:ulrike.krewer@kit.edu) (U. Krewer).

interface [9]. The appearance of faradaic currents at anodic potentials before the onset of the OER is either attributed to adsorption of additional hydroxy groups [10–13] on the hydrous iridium surface or to deprotonation steps [14–16]. X-ray emission spectroscopy allowed to detect increasing overall oxygen content in the hydrous Ir material and the electron diffraction pattern suggests formation of pseudo-rutile IrO<sub>2</sub> [17]. This finding matches with in-situ X-ray absorption (XAS) measurements, since in acid media it is concluded that the intermediate state at approximately 1.05 V vs RHE fits the Ir–O distance of crystalline IrO<sub>2</sub> [18]. According to in-situ X-ray photoelectron spectroscopy (XPS) analysis in different binding energies of the O 1s level, there is a decreasing hydroxy and an increasing oxide content with increasing potential in the range of approximately 0 V up to 1.5 V vs RHE [16]. In the near surface region, the observation of adsorbed hydroxide and oxygen is additionally confirmed using atom probe tomography and could furthermore be correlated to a metastable state with an IrO and OH ratio of roughly 1 [8].

XPS analysis reveals the co-existence of +III and +IV oxidation states [19–21]. The picture of the surface transformation process is complemented by XAS analysis, which allows to differentiate three main potential regions: (i) between 0.2 V and 0.7 V vs RHE, multiple studies agree on an oxidation state of +III [20,22,23]. (ii) The potential range ongoing from 0.7 V up to approximately 1.1 V shows mainly Ir(IV) [23,24]. (iii) At potentials higher than 1.1 V vs RHE, an increasing oxidation state up to +V and even higher can be obtained [22,23]. During the OER different oxidation states, namely +III, +IV and +V were detected [23,25]. Based on experimental results one is able to formulate reaction mechanisms for the ad- and desorption processes [16,26] as well as for the OER [9,27] (details see Section 2.2).

To complement this experimental findings, modelling methods are used to extend the analysis by identifying the mechanism, quantify its kinetics and prove thermodynamic consistency. Energetically favourable intermediate states on metals [28] and oxides [29,30] are extensively postulated using calculations based on density functional theory (DFT). This method is limited to distinct states and not able to describe reaction kinetics and its behaviour under experimental conditions. In contrast, microkinetic modelling based e.g. on Butler-Volmer theory and including surface coverages, uses multiple rate equations of reactions and processes to calculate performance relevant values (e.g. current, surface coverages and rates) and their behaviour. A direct validation with the experiment is possible. This method was applied on Ir oxide to study the OER mechanism [31], dissolution pathways [32], to simulate electrolyzers [33] on a multiscale or to describe the OER mechanism in general [34]. To simplify the calculation either one of the assumptions was and is commonly taken into account [35]: (i) non rate determining steps are expected in quasi-equilibrium or (ii) relevant variables, mostly the concentration of intermediates, are required to remain constant over time and fixed at steady-state. But a lot of downsides are reported recently e.g. the underestimation in number of unique tafel slopes [36] or a lack of identifiability of kinetic parameters [37] and the rate determining step [34], especially if it is similarly slow to a second last rate or it is substituted due to shift in potential [35].

As obviously quasi-equilibrium and steady-state assumptions lead to problems in microkinetic analysis, a more complex full dynamic analysis is advisable. Such models will then also allow to simulate and quantitatively analyse the experimentally frequently used dynamic measurements. Modeling without quasi-equilibrium and steady-state assumptions is crucial to perform simulations with dynamic input values with no further restraints. Resulting models can reproduce multiple dynamic experiments such as cyclic voltammetry (CV) [38–40] and potentiostatic mass transfer responses [41,42], electrochemical impedance spectroscopy

[43–45] or nonlinear frequency methods [46,47]. They allow more precise interpretation of measurements through detailed analysis of processes at the surface. Such analyses would also be beneficial for understanding the OER, but have not been conducted so far. A first study of such kind is presented for OER at hydrous iridium in this manuscript. We present carefully conducted CV experiments, the deduction of two most likely reaction mechanisms from literature and a model-based study on the microkinetics. This includes changes in surface coverage with multiple adsorbed species and the formation of reduced species at highly oxidative potential. The results resolve how the potential affects the reaction rates and changes the rate limiting steps. Further, the thermodynamic properties are derived from the model, which allows to bridge the gap between experiments and ab initio calculations such as density functional theory and molecular dynamics based simulations.

## 2. Method

### 2.1. Experimental setup

All electrochemical experiments were carried out in a PTFE cell combined with a rotating disc electrode (RDE) setup from PINE Research Instrumentation Inc., connected to a Gamry Reference 600+ potentiostat. Deionized water (Merck MilliQ, 18.2 MΩ) was used as solvent and for extensively rinsing the cell prior to the measurements. Sulfuric acid ROTIPURAN®Supra 95% from Carl Roth GmbH + Co. KG was purchased to produce the 0.1 M H<sub>2</sub>SO<sub>4</sub> electrolyte solution. The working electrode consisted of a polycrystalline iridium cylinder produced and pre-polished by Mateck GmbH and embedded planar into a PEEK electrode holder. A PTFE shroud assures sealing and backside gold pin electrical conductivity with the RDE rotator shaft.

The experiments were performed as follows: prior to the measurement the available circular electrode area  $A = 0.1963 \text{ cm}^2$  was polished with 0.05 μm Aluminium containing polish media to remove remaining hydrous film. The cell was filled with 200 ml electrolyte solution and purged with Argon ( $\geq 99.996\%$ ) for 10 min before and during the complete experiments. Platinum wire counter and HydroFlex reversible hydrogen reference electrode (RHE) from Gaskatel mbH were inserted directly in the cell. The hydrous iridium film was produced by cycling the polycrystalline iridium electrode 100 times in the potential scan range from  $E_{\text{RHE}} = 0.05 \text{ V}$  to 1.55 V with a potential rate of  $dE/dt = 500 \text{ mV s}^{-1}$ . This method is widely used in multiple studies [15,48,49]. Once the film has been established, potential driven electrochemical impedance spectroscopy (EIS) was performed at open circuit potential with frequencies ranging from  $f = 10^5 \text{ Hz}$  to  $10^{-1} \text{ Hz}$  with an amplitude of  $\hat{E} = 10 \text{ mV}$ . Subsequently, three consecutive cyclic voltammograms (CV) were measured with potential rates  $dE/dt = [500, 200, 100, 50, 20, 10] \text{ mV s}^{-1}$  in between potentials of  $E_{\text{RHE}} = 0.3 \text{ V}$  and 1.6 V. All potentials are given versus RHE, if not otherwise stated.

### 2.2. Mechanistic assumptions

In order to establish a micro kinetic model for the OER at hydrous iridium, the assumption of at least one mechanism is required. Fig. 1 provides an overview of literature-proposed mechanisms including the respective pathways and oxidation states. While 1 a) to 1 c) are formulated based on experimental findings on hydrous iridium [7,16,23,50,51], mechanism 1 d) is widely used in DFT calculations of the OER on metal and oxide catalysts e.g. on rutile IrO<sub>2</sub> [29,30,52].

Since the output of a microkinetic model depends strongly on the assumed mechanism, a careful validation of the reaction mechanisms provides the basis to set up the model successfully. There-

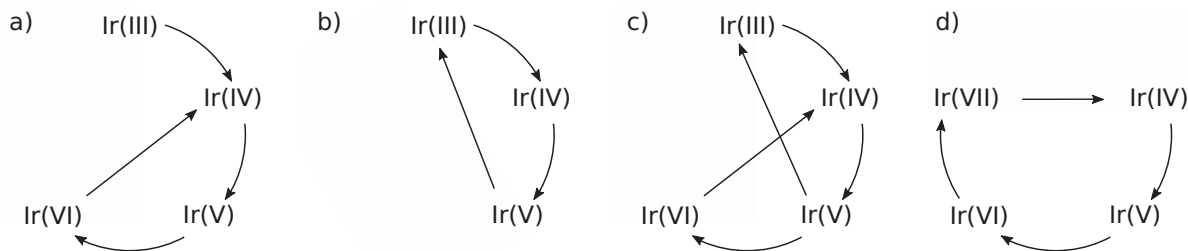


**Fig. 1.** Mechanisms proposed for surface oxidation reaction steps and OER for hydrous Ir by a) Kötz et al. [16], b) Cherevko et al. [7], Minguzzi et al. [23] and Steegstra et al. [50], c) Kasian et al. [51] and d) for rutile IrO<sub>2</sub> by Rossmeisler et al. [29] and Klyukin et al. [52]

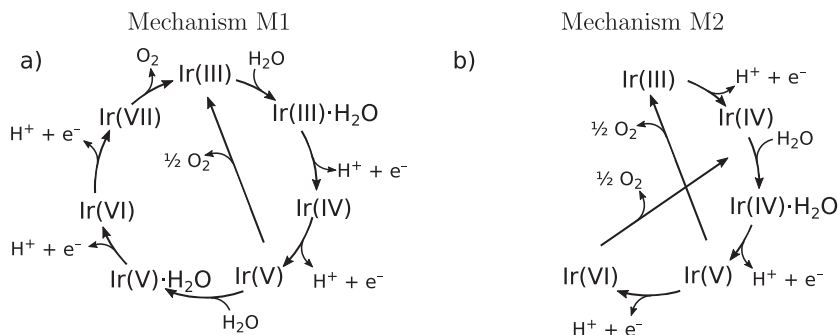


**Fig. 2.** a) Visualization of the reaction mechanism M1 based on assumptions published for DFT calculations on several oxides. b) Scheme of mechanism M2 derived by Kasian et al. [51] based on experimental results of hydrous iridium.

fore, an evaluation is done by comparing the mechanisms with four major experimental findings. (i) CV results from literature [7,12,16,17] and own experiments (see Section 3.1) exhibit at least two distinct electron transfer reactions in addition to the exponential onset of the OER. This requires a minimum of three distinguishable electrochemical reactions to be present in the overall mechanism. (ii) In situ XPS and XAS studies [16,22,23] imply oxidation states ranging from +III up to at least +VI. Additionally, XAS findings [23] state the occurrence of reduced oxidation state +III even at high potentials of approximately 1.6 V. (iii) XPS measurements [16,25] reveal an increasing amount of covalent oxygen bindings with increasing potential. Iridium hydroxide bonds are present at several potentials and even in the OER region. (iv) Atom probe tomography detected the material composition to contain IrO and OH with a ratio of roughly 1:1 [8]. According to these results, the hydrous Ir consists of the species IrO(OH) initially.

In the following, we formulate reaction mechanisms that take the various theories and findings into consideration. As the experimental and DFT-derived mechanisms deviate significantly, we consider it proper to evaluate and compare both concepts. We firstly setup a reaction mechanism inspired by the DFT studies 1 d) on rutile IrO<sub>2</sub> that takes into account the findings (i) to (iv). All reactions are adopted accordingly, but instead of Ir(IV) ≡ IrO<sub>2</sub>, the initial species is defined as Ir(III) ≡ IrO(OH), the hydrous iridium (Fig. 2 a)). Species with oxidation states of +III are oxidized stepwise up to +VII or +V and reduced back to +III while oxygen is released as a single site or a dual site step. Herewith, one is able to formulate a first mechanism (M1) which can be described by eight reaction steps (eq. 1–8) and is closely related to the mechanism widely used in DFT calculations for several oxides (Fig. 1 d)).

Additionally, to respect the studies that experimentally derived OER mechanisms 1 a) - 1 c), a second mechanism was taken into account for our kinetic modelling. The mechanism in Fig. 1 a) contradicts with finding (iii), since the reduced +III oxidation state is

not present in the OER circle. Mechanism 1 b) contains only two electrochemical steps and, therefore, might be able to describe the OER, but not the potential range prior to the OER completely. In principle, the mechanism in Fig. 1 c) is a combination of the two previous ones and, thus, is in line with all major experimental findings. We therefore choose the mechanism written down by Kasian et al. [51] as the second evaluated mechanism (M2). It is displayed in Fig. 2 b) and can be described by six reactions (eq. 9–14).

Since H<sub>2</sub>O adsorption on oxides was found to be energetically favourable [30,53], it is implemented as an individual chemical step, decoupled from further electrocatalytic proton coupled electron transfer (PCET). Both mechanisms, M1 and M2, are visualized in Fig. 2, starting with the initial hydrous iridium species Ir(III) ≡ IrO(OH) found by atom probe tomography. They provide a sound basis for formulating the kinetic models presented in the following.

Mechanisms M1 and M2 are converted into a form consisting of active catalyst sites, denoted with \*, on which single surface species can adsorb, desorb and react. This enables microkinetic modelling and balancing of the species.

Mechanism M1 * ≡ Ir(OH) ≡ Ir(III)		Mechanism M2 * ≡ Ir(O) ≡ Ir(IV)	
* + H <sub>2</sub> O $\xrightleftharpoons{r_1}$ *H <sub>2</sub> O	(1)	*H $\xrightleftharpoons{r_1}$ * + H <sup>+</sup> + e <sup>-</sup>	(9)
*H <sub>2</sub> O $\xrightleftharpoons{r_2}$ *OH + H <sup>+</sup> + e <sup>-</sup>	(2)	* + H <sub>2</sub> O $\xrightleftharpoons{r_2}$ *H <sub>2</sub> O	(10)
*OH $\xrightleftharpoons{r_3}$ *O + H <sup>+</sup> + e <sup>-</sup>	(3)	*H <sub>2</sub> O $\xrightleftharpoons{r_3}$ *OH + H <sup>+</sup> + e <sup>-</sup>	(11)
*O + H <sub>2</sub> O $\xrightleftharpoons{r_4}$ *OH <sub>2</sub> O	(4)	*OH $\xrightleftharpoons{r_4}$ *O + H <sup>+</sup> + e <sup>-</sup>	(12)
*OH <sub>2</sub> O $\xrightleftharpoons{r_5}$ *OOH + H <sup>+</sup> + e <sup>-</sup>	(5)	2*O $\xrightleftharpoons{r_5}$ 2* + O <sub>2</sub>	(13)
*OOH $\xrightleftharpoons{r_6}$ *OO + H <sup>+</sup> + e <sup>-</sup>	(6)	2*OH $\xrightleftharpoons{r_6}$ 2*H + O <sub>2</sub>	(14)
2*O $\xrightarrow{r_7}$ 2* + O <sub>2</sub>	(7)		
*OO $\xrightarrow{r_8}$ * + O <sub>2</sub>	(8)		

### 2.3. Microkinetic model equations

The reaction kinetic modeling of mechanisms M1 and M2 is methodically inspired by previous studies [39,44,54,55] and based on rate equations for chemically  $r_C$  and electrochemically  $r_E$  driven reactions Eq. 15 - (18).

$$r_{C,+i} = k_{C,+i} \cdot \prod_{j \in S} (a_j^{v_{+ij}} \cdot \theta_j^{v_{+ij}} \cdot f_+(\theta)) \quad (15)$$

$$r_{E,+i} = k_{E,+i} \cdot \prod_{j \in S} (a_j^{v_{+ij}} \cdot \theta_j^{v_{+ij}} \cdot f_+(\theta)) \cdot \exp\left(\frac{\beta z F}{RT} \cdot E\right) \quad (16)$$

$$r_{C,-i} = k_{C,-i} \cdot \prod_{j \in S} (a_j^{v_{-ij}} \cdot \theta_j^{v_{-ij}} \cdot f_-(\theta)) \quad (17)$$

$$r_{E,-i} = k_{E,-i} \cdot \prod_{j \in S} (a_j^{v_{-ij}} \cdot \theta_j^{v_{-ij}} \cdot f_-(\theta)) \cdot \exp\left(\frac{-(1-\beta)zF}{RT} \cdot E\right) \quad (18)$$

Forward  $r_{+i}$  and backward  $r_{-i}$  rates are calculated separately, with the use of reaction rate constants  $k_{+i}$  and  $k_{-i}$ , the activities  $a_j$ , surface coverages  $\theta_j$  for the species  $j \in \{\text{H}_2\text{O}, \text{OH}, \text{O}, \text{OH}_2\text{O}, \text{OOH}, \text{OO}\}$  and the electrode potential  $E$ . Adsorption functions  $f_+$  and  $f_-$  account for non-idealities of adsorption processes that affect the kinetics. As in all assumed electrochemical reactions  $r_E$ , only one electron is transferred, the symmetry factor  $\beta$  is assumed to be 0.5 and the electron transfer number set to  $z = 1$ . Stoichiometric coefficients  $v_{ij}$  define the contribution species  $j$  in reaction  $i$ . The electrode coverage  $\theta_j$  of surface-bound intermediates  $j$  is taken into account and since for hydrous iridium the broadened peak behaviour [50] implies surface coverage dependent adsorption energies with species interaction, a van der Waals adsorption isotherm is assumed [56–58]. This considers an areal spacing of surface sites and the interaction of adsorbed species [58]. For an in-depth discussion see Appendix A. The adaptation of this adsorption behaviour into the reaction equations, which was done in an analogous manner for Frumkin/Temkin adsorption [59,60], results in the functions  $f_+$  and  $f_-$  for forwards and backwards reactions respectively:

$$f_+ = \exp\left(\beta \left[ g_j \cdot \theta_j^{v_{+ij}} - g_j \cdot \theta_j^{v_{-ij}} + \frac{\theta_j^{v_{+ij}}}{\theta_j^{v_{-ij}}} - \frac{\theta_j^{v_{-ij}}}{\theta_j^{v_{+ij}}} \right]\right) \quad (19)$$

$$f_- = \exp\left(- (1-\beta) \left[ g_j \cdot \theta_j^{v_{+ij}} - g_j \cdot \theta_j^{v_{-ij}} + \frac{\theta_j^{v_{+ij}}}{\theta_j^{v_{-ij}}} - \frac{\theta_j^{v_{-ij}}}{\theta_j^{v_{+ij}}} \right]\right) \quad (20)$$

The dynamic behaviour during a CV is arising by the single potential dependent reaction and sorption processes, which trigger the change in surface coverage  $\theta_j \in [0, 1]$  of the intermediate species over time  $t$ . To account for this, a species balance for all adsorbed species is formulated which contains besides the reactions  $r_i$  also the density of active sites  $\rho$  of the catalytic surface:

$$\frac{d\theta_j}{dt} = \frac{1}{\rho} \sum_i (r_{+i}^{v_{+ij}} - r_{-i}^{v_{-ij}}) \quad (21)$$

The charge at the surface is balanced using a dynamic charge balance containing charge accumulation in the double layer  $dq/dt$  with its capacitance  $C_{DL}$ , charge transport  $j$  and sources and sinks due to electrochemical reactions:

$$\frac{dq}{dt} = C_{DL} \cdot \frac{dE}{dt} = j(t) - zF \sum_i (r_{E,+i}(t) - r_{E,-i}(t)) \quad (22)$$

Potential drop in the electrolyte layer is accounted for by correcting the externally applied potential  $E_{\text{ext}}$  with the current density  $j$ , geometric electrode area  $A$  and electrolyte resistance  $R_{EL}$ :

$$E = E_{\text{ext}} - jAR_{EL} \quad (23)$$

The overall equation system can be solved for dynamic potential  $E_{\text{ext}} = E_{\text{ext}}(t)$ . Appendix B contains the full set of reaction kinetic equations and species balances for mechanisms M1 and M2.

The formal mean oxidation state  $OS_m$  is calculated by summing up the coverage weighted oxidation states of all assumed species  $j$ :

$$OS_m = \sum_j \theta_j \cdot OS_j \quad (24)$$

### 2.4. Performing simulation and model parameter identification

The electrochemical model of Section 2.3 equations were implemented in MATLAB and the respective set of ordinary differential equations solved using the ode23s algorithm with a given set of kinetic parameters over time. Simulations were performed by applying a constant input potential rate within the same voltage range as in the experiment.

Parametrisation of the model equations is done based on values directly gained from experiments and by optimizing the model output on experimental CV curves. Easily accessible parameters temperature  $T = 298.15$  °C and geometrical electrode area  $A = 0.1963$  cm<sup>2</sup> are inserted directly in the model. Electrolyte resistance  $R_{EL} = 19$  Ω was gained by measuring with impedance spectroscopy and quantifying the real component at high frequency of 10<sup>5</sup> Hz. We assume a constant double layer capacitance of  $C_{DL} = 25$  μF following experimental findings in literature [7]. The activity of liquid species at the interface is assumed to be equalised with its respective bulk values due to fast transport. In addition, their concentrations in the electrolyte are very high compared to consumption and production, so that the steady state assumption is plausible. Therefore, relevant electrolyte activities are set to a constant value of  $a_{\text{H}_2\text{O}} = 1$  and  $a_{\text{H}^+} = c_{\text{H}^+}/c^0 = 0.1$  with the standard concentration  $c^0 = 1$  mol/L to replicate the experimental specifications of the 0.1 M aqueous solution. Proton activity, reported with values of 0.078 [61] and 0.132 [62], might deviates from the assumed value and, thus, influences the parametrized kinetic rate constants of the protonation steps. The constants correlate linearly and perfectly negative with a possible deviation in proton activity as one proton is transferred each step. Nevertheless, further results such as reaction rates and coverages are unaffected. Standard Gibbs free reaction energy values are as well unaffected due to the correction with respect to electrochemical standard conditions.

The kinetic rate constant of the oxygen adsorption steps for M1  $k_{-7}$  and  $k_{-8}$  and for M2  $k_{-5}$  and  $k_{-6}$  are set to zero since the oxygen evolution is assumed to be irreversible due to its high reaction energies. The remaining rate constant values  $k_i$ , the dimensionless adsorption parameter  $g_j$  and the density of active sites  $\rho$  are identified with a optimization algorithm using the third experimental CV curve at  $dE_{\text{ext}}/dt = 200$  mV s<sup>-1</sup>. This scan rate was chosen as it gives well pronounced and clearly distinguishable features in the experimental data (see Section 3.1). The algorithm modifies all parameters successively by a defined value  $\pm m$  in case the variation results in a decrease of the root mean square error (RMSE, Eq. 25). This was performed repeatedly until RMSE reaches its minimum and iterated for several modification values  $m \in \{10^{-1}, 10^{-2}, 10^{-3}, 10^{-4}\}$  for  $g_j$ ,  $10^m$  for  $k_i$  and  $10^{0.1 \cdot m}$  for  $\rho$ .

$$RMSE = \sqrt{\frac{\sum_n (j(E_n) - j_{\text{exp}}(E_n))^2}{n}} \quad (25)$$

Since the amount of kinetic parameters is very high, the algorithm for parameter identification uses a two step procedure. First, the rate constants and adsorption coefficients of reactions  $i \in \{1, 2\}$  for M1 and reaction  $i \in \{1\}$  for M2 as well as the density of active sites were identified by minimizing the RMSE in the potential range  $0.45$  V  $< E_{\text{ext}} < 1.1$  V. This is applicable since the reactions

are assumed to occur in this region and be responsible for the observed current peaks. Hence, its parameters are sensitive in this potential region. In a second step, the rest of the rate constants and adsorption coefficients of reactions  $i \in \{3, 4, 5, 6, 7, 8\}$  for M1 and reaction  $i \in \{2, 3, 4, 5, 6\}$  for M2 were identified by minimizing the RMSE at potentials  $E > 1.3$  V. With this procedure a set of parameters was obtained, which is able to describe the experimental data at  $dE_{ext}/dt = 200$  mV s<sup>-1</sup> with sufficient low RMSE.

### 3. Results & discussion

In the following, we will firstly discuss the experimentally recorded CV curves and highlight the characteristic features. Then, the results of the parametrisation processes will be given and explained. Simulation results and the quantification of microkinetic insights such as reaction rates and coverage of intermediate species are described and discussed. At the end of this chapter, we deduce thermodynamic parameters from the simulations and compare them with literature.

#### 3.1. Experimental results

Cyclic voltammograms on hydrous Ir films were recorded in the potential range between  $E = 0.35$  V and 1.6 V vs RHE in 0.1 M H<sub>2</sub>SO<sub>4</sub>. The results for each 3<sup>rd</sup> cycle are given in Fig. 3. They exhibit four features in current ( $A_0$ ,  $A_1$ ,  $A_2$  and OER) that arise from different electrocatalytic processes: (i) the first anodic peak  $A_0$  at  $E = 0.6$  V is related to the oxidation of the underlying metallic bulk Ir [63]. (ii) Hydrous film oxidation from Ir(III) to Ir(IV) via a proton coupled electron transfer step results in the broadened peak  $A_1$  with an anodic maximum at approximately  $E = 0.95$  V [16,64]. (iii) A further proton coupled electron transfer (PCET), resulting in a change of oxidation state from Ir(IV) to Ir(V) [16,23], takes place at  $E = 1.4$  V and is seen in the feature  $A_2$  prior to (iv) the OER, which is identified with the exponential increase in current at  $E = 1.5$  V. Sufficient peak separation and the correlation with a change in oxidation state by one of each of the features  $A_1$  and  $A_2$  are observed. This allows for the conclusion that the present features are not linked to different oriented surfaces. The results are, therefore, in agreement with the widely accepted assumption of a porous and amorphous structured material [8,65]. As can be seen, the different scan rates do not cause a qualitative change in the spectrum; all peaks are still visible in the same potential area. The most pronounced peaks are obtained at 200 mV s<sup>-1</sup>. Analysis of electrochemical impedance spectra at open circuit

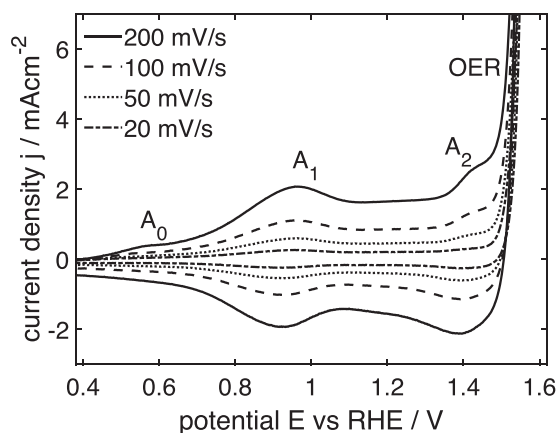


Fig. 3. Experimentally recorded cyclic voltammogram of hydrous Ir in 0.1 M H<sub>2</sub>SO<sub>4</sub> for various scan rates. The third cycle is displayed, respectively. Characteristic features  $A_0$ ,  $A_1$ ,  $A_2$  and OER are marked.

potential and high frequency of  $f = 10^5$  Hz reveals an electrolyte resistance of  $R = 19$   $\Omega$ . There is no impact or limitation due to diffusion in the electrolyte, since rotation of the electrode shows no significant change in current density over the full CV potential range.

#### 3.2. Model parameter results

As explained above, several model parameters are gained from experiments via model based identification with an input potential rate of  $dE/dt = 200$  mV s<sup>-1</sup>. CV simulations using the identified parameter set for M1 and the parameter set for M2 are in good agreement with the experimental data, as they reproduce the main features observed in the experiment shown in Fig. 4 a) and b). We will firstly discuss the simulation with a scan rate of 200 mV s<sup>-1</sup>. The RMSE values of the first adsorption process  $A_1$  ( $0.75 \leq E \leq 1.1$  V) equals 0.14 mA cm<sup>-2</sup> for M1 and 0.13 mA cm<sup>-2</sup> for M2 and displays the high accuracy. At the second adsorption peak  $A_2$  and OER ( $1.3$  V  $\leq E$ ) the respective values for both mechanisms 0.31 (M1) and 0.41 (M2) mA cm<sup>-2</sup> are slightly higher. Major discrepancies are visible at  $E < 0.7$  V and  $1.1 < E < 1.3$  V leading to RMSE values of 0.27 (M1) and 0.37 mA cm<sup>-2</sup> (M2) for the full CV. The features in the low potential region around and below  $A_0$  are known to correlate with the reduction of the bulk metallic Ir [63]. This process is not considered in the model, leading thus to the discrepancy at  $E < 0.7$  V. The second potential region ( $1.1 < E < 1.3$  V) might cover either a non-faradaic influence or an additional adsorption process, the model fails to reproduce this feature and, to the best of our knowledge, neither does any experimental report have an explanation for the behavior observed in this region. Regardless, the discrepancy is comparably small. Both models are also similarly able to reproduce the experimental CV features when changing the scan rate shown Fig. 4 c) and d). Overall we conclude that both mechanisms can reproduce the dynamic experimental electrochemical data very well at different potential rates. Thus a discrimination needs additional analysis, as discussed in Section 3.3.

In the following, we discuss the identified parameters for mechanism M1 and M2 listed in Table 1. The obtained density of accessible and active sites is roughly 2 orders of magnitude higher compared to the value reported in literature for a (110) oriented surface of IrO<sub>2</sub>  $\rho_{IrO_2(110)} = 8.3 \cdot 10^{-6}$  mol m<sup>-2</sup> [66]. The value is plausible as hydrous Ir is forming multiple electrochemically active layers during the cyclic treatment [17] prior to the measurement. Although the three-dimensional film is continuously growing with each cycle and with this the number of active sites, the changes during one cycle are rather small. With respect to a preceding study [67] the thickness of the experimentally produced film is estimated to be 3.7 nm after 100 cycles. This results in a volumetric density of active sites in the film of 0.13 mol cm<sup>-3</sup>. Further it is found, that the adsorption parameter  $g$  does influence the van der Waals adsorption terms quite significantly. In some reactions  $r_i$  (M1:  $i \in \{2, 3\}$ ; M2:  $i \in \{1, 2, 3\}$ ), high  $g$  values lead to flattened, but broader faradaic current peaks  $A_1$  and  $A_2$  in the potential region prior to the OER onset. As shown in Appendix A, neither Langmuir nor Volmer adsorption allow for a broad peak. Thus, the assumption of a van der Waals isotherm seems to be justified including the underlying assumption of areal spacing of surface sites and the interaction of adsorbed species.

Kinetic rate constants  $k$  of the electrochemical deprotonation steps follow a clear tendency: forward reaction rate constants are lower by more than 20 times the order of magnitude compared to their backward counterparts. This is plausible due to the fact, that potential is given versus reversible hydrogen reference electrode and not to the equilibrium potential of each process. As the reaction rate of chemical reaction are rather independent of the electrochemical potential, consequently, the respective rate con-

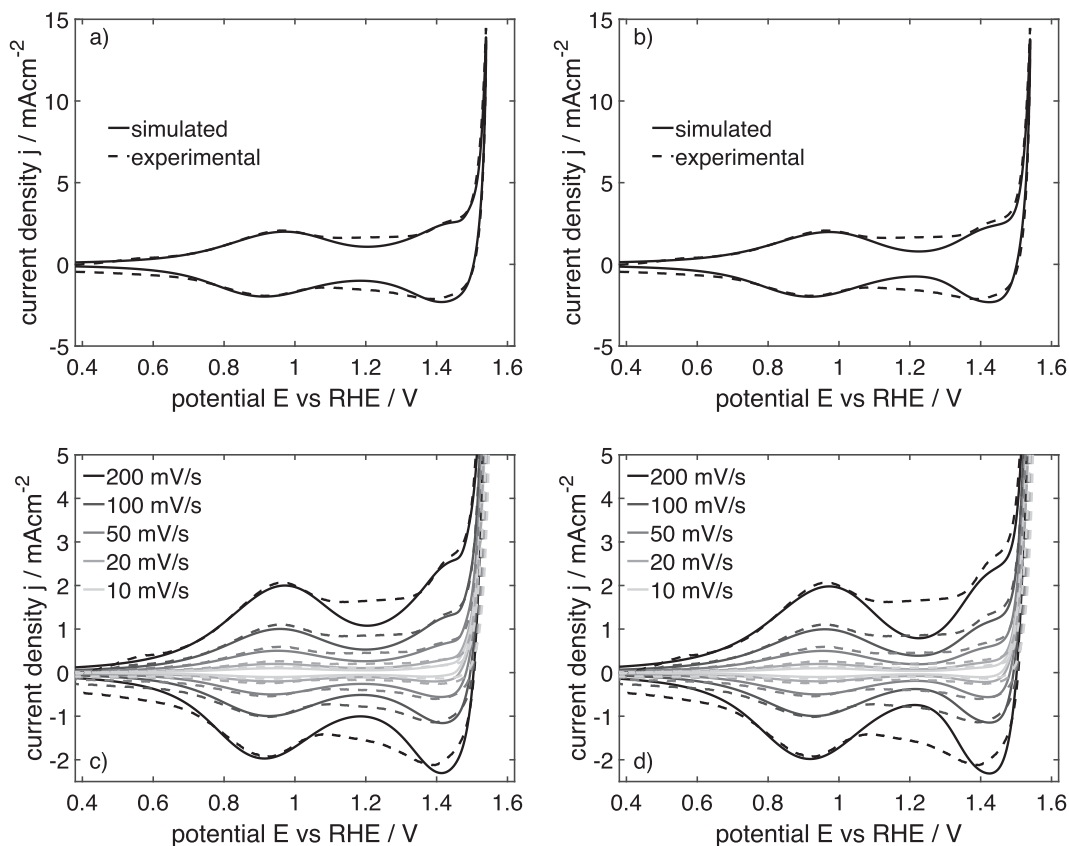


**Fig. 4.** Simulated CV curves resulting from the parameter identification process at potential rate of 200 mV s<sup>-1</sup> of a) mechanism M1 and b) mechanism M2 in comparison to the third cycle of the experimental results. Using the identified parameters at 200 mV s<sup>-1</sup>, simulation of CV curves at different potential rate  $dE/dt = [200, 100, 50, 20, 10]$  mV s<sup>-1</sup> of c) mechanism M1 and d) mechanism M2 are conducted (line) and plotted with the respective experimental data (dashed line).

**Table 1**  
Parameter values identified from cyclovoltammogram for mechanisms M1 and M2.

index	Mechanism M1				Mechanism M2			
	$k_i$	$k_{-i}$	$g_j$	$\rho$	$k_i$	$k_{-i}$	$g_j$	$\rho$
		mol m <sup>-2</sup> s <sup>-1</sup>	-	mol m <sup>-2</sup>		mol m <sup>-2</sup> s <sup>-1</sup>	-	mol m <sup>-2</sup>
1	$1.0 \cdot 10^{-5}$	$6.3 \cdot 10^{-28}$	0.9	$4.6 \cdot 10^{-4}$	$9.4 \cdot 10^{-12}$	$1.1 \cdot 10^6$	3.9	$5.0 \cdot 10^{-4}$
2	$1.0 \cdot 10^{-11}$	$7.1 \cdot 10^5$	3.6		$1.9 \cdot 10^{-4}$	$1.3 \cdot 10^2$	4.0	
3	$1.3 \cdot 10^{-14}$	$1.5 \cdot 10^{12}$	3.6		$1.4 \cdot 10^{-13}$	$2.7 \cdot 10^{11}$	6.5	
4	$1.0 \cdot 10^{-13}$	$1.9 \cdot 10^8$	0.3		$2.0 \cdot 10^{-16}$	$3.7 \cdot 10^{13}$	1.2	
5	$7.8 \cdot 10^{-15}$	$8.8 \cdot 10^{13}$	0.1		$1.0 \cdot 10^0$		0.0	
6	$1.6 \cdot 10^{-12}$	$1.8 \cdot 10^{15}$	0.3		$2.4 \cdot 10^{-6}$		0.0	
7	$7.8 \cdot 10^{-12}$		0.0					
8	4.4		0.0					

stants deviate from this trend. The impact of the parameter on the microkinetics and detailed discussion about the reaction rates the coverages and the thermodynamics of the system is given in the following for both mechanisms M1 and M2 separately.

### 3.3. Microkinetic insights of mechanism M1

Fig. 5 a) shows the surface coverages and b) the reaction rates calculated for mechanism M1. The first and second PCET steps, i.e. the oxidation resulting to adsorbed species \*OH and \*O dominate the pre OER potential region. Both can be assigned to define the respective current peaks A<sub>1</sub> and A<sub>2</sub> reaching effective reaction rates  $r_i = r_{+i} - r_{-i}$  of  $r_2 = 0.19$  and  $r_3 = 0.24$  mmol m<sup>-2</sup> s<sup>-1</sup>. In this region all other reactions are slow with effective rates below 0.05 mmol m<sup>-2</sup> s<sup>-1</sup>. At potentials  $E > 1.5$  V, O<sub>2</sub> is predominantly forming via the single site pathway ( $*O \xrightarrow{r_8} * + O_2$ ). The effective oxygen production rate reaches its maximum of  $r_8 = 0.36$  mmol m<sup>-2</sup>

s<sup>-1</sup> at the highest simulated potential. Production rate via the dual site reaction pathway  $2*O \xrightarrow{r_7} 2* + O_2$  in which two oxygen atoms from neighboring sites form one oxygen molecule as assumed in reaction step 7 is calculated to  $r_7 < 0.29 \cdot 10^{-6}$  mmol m<sup>-2</sup> s<sup>-1</sup> and thus multiple orders of magnitude slower. Whereas during lower potentials prior to the OER, rates of reactions occur individually, the increase to potentials in the OER region comes with an increase of multiple reaction rates. This is clearly visible in the inset of Fig. 5 b). Except for the dual site step, all other reactions in the cycle converge to the same curve, which allows a continuous oxygen evolution under participation of all oxidation states. In the potential range from  $0.4 \text{ V} < E < 1.2 \text{ V}$ , reaction  $*H_2O \xrightarrow{r_2} *OH + H^+ + e^-$  is predominant, which results in a high amount of present \*OH  $\equiv$  Ir(IV) of 25.1%. At higher potentials above 1.2 V, the second deprotonation reaction rate  $*OH \xrightarrow{r_3} *O + H^+ + e^-$  increases significantly and produces considerable amount of adsorbed \*O. This is

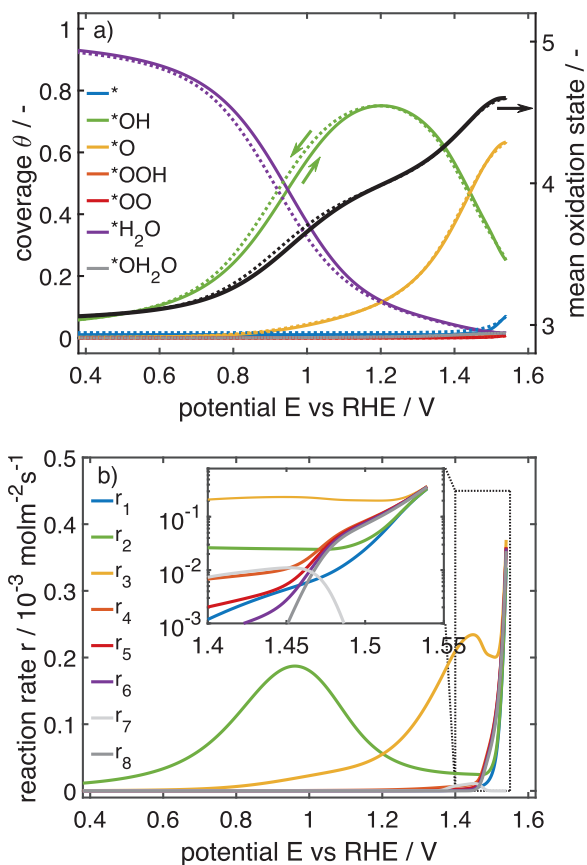


**Fig. 5.** Simulation results of mechanism M1. a) Coverage of intermediate surface species with dynamically upwards (bold lines) and downwards (dotted lines) sweeping potential on the left axis. The mean iridium oxidation state value is indicated by the bold black line with respect to the right axis. b) Effective reaction rates during the forward scan of a CV.

additionally supported by the fact, that chemical H<sub>2</sub>O adsorption via step  $*O + H_2O \xrightarrow{r_4} *OH_2O$  is balanced heavily towards the side of the educt. The resulting availability of  $*O$  gives rise to  $r_7$  and the OER. The minor extent of the oxygen production via this pathway might be explained by high activation barriers as there are two sites involved. At potentials above 1.45 V the rate of this dual site pathway rapidly decreases because the competing pathway including the steps  $r_4$ ,  $r_5$ ,  $r_6$  and  $r_8$  become favourable. The inset of Fig. 5 b) shows all four reaction rates converging and ascending exponentially. The increase in potential accelerates especially the effective rates of both deprotonation steps  $*OH_2O \xrightarrow{r_5} *OOH + H^+ + e^-$  and  $*OOH \xrightarrow{r_6} *OO + H^+ + e^-$ . In consequence the chemical adsorption rate  $r_4$  follows to compensate for the depletion of  $*OH_2O$  and oxygen is chemically evolving with a rate  $r_8$  directly linked to the amount of produced  $*OO$ .

Regardless of the increase in reactions  $r_4$ ,  $r_5$ ,  $r_6$  and  $r_8$ ,  $*O \equiv Ir(V)$  remains the mayor available intermediate species and covers 63.4% of the surface sites. This is explained only by a limitation of the overall cyclic process by the chemical H<sub>2</sub>O adsorption  $r_4$ . H<sub>2</sub>O adsorption, therefore, is a crucial step. This becomes additionally visible in the slight increase in the amount of free surface sites  $*$  at potentials above 1.5 V up to a total amount of 7.0 % at 1.55 V. In Fig. 5 a) slow H<sub>2</sub>O adsorption  $r_1$  forces the first deprotonation reaction rate  $r_2$  to undercut the single site OER rate  $r_8$ . As  $r_1$  tends to converge  $r_8$  from below and the reduced intermediate species  $* \equiv Ir(III)$  is produced, this H<sub>2</sub>O step is limiting at high potentials.

Overall, for mechanism M1 one can conclude, that the definition of the rate determining step becomes challenging in the dy-

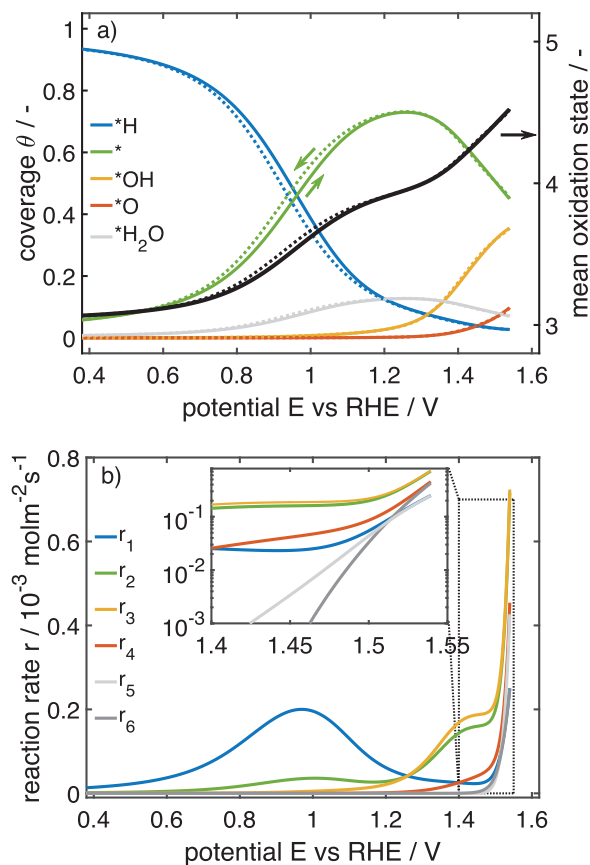


**Fig. 6.** Simulation results of mechanism M2. a) Coverage of intermediate surface species with dynamically upwards (bold lines) and downwards (dotted lines) sweeping potential on the left axis. The mean iridium oxidation state value is indicated by the bold black line with respect to the right axis. b) Effective reaction rates during the forward scan of a CV.

namic context. An accumulation of three species Ir(III), Ir(IV) and Ir(V) is occurring at high potentials > 1.5V relevant for electrolysis. This is a clear sign, that the subsequent reactions  $r_1$ ,  $r_4$  and  $r_5$ , which use these species as reactants are slow and define the overall turnover.

### 3.4. Microkinetic insights of mechanism M2

For mechanism M2, surface coverages and reaction rates are shown in Fig. 6 a) and b) respectively. In analogon to mechanism M1, there are distinctive regions in the pre OER potential region in which one or two reactions are dominant. At potentials below 1.2 V, deprotonation via reaction  $*H \xrightarrow{r_1} * + H^+ + e^-$  describes the feature A1, and the slow H<sub>2</sub>O adsorption leads to an accumulation of  $* \equiv IrO_2 \equiv Ir(IV)$  species. Above 1.2 V, H<sub>2</sub>O adsorption  $* + H_2O \xrightarrow{r_2} *H_2O$  and the deprotonation  $*H_2O \xrightarrow{r_3} *OH + H^+ + e^-$  increase significantly and are the major observed reactions. Hence, the amount of present  $*OH \equiv Ir(V)$  rises with higher potentials and enables oxygen to evolve chemically via the dual site pathway  $2*OH \xrightarrow{r_5} 2*H + O_2$ . The oxygen evolution via this pathway reaches its highest rate of  $r_5 < 0.25 \text{ mmol m}^{-2} \text{ s}^{-1}$  at the highest simulated potential. The second OER pathway  $2*O \xrightarrow{r_6} 2* + O_2$  becomes dominant at potentials above 1.52 V, since potential driven deprotonation  $*OH \xrightarrow{r_4} *O + H^+ + e^-$  provides sufficient amount of  $*O \equiv Ir(VI)$ . Both rates  $r_4$  and  $r_6$  converge at highest potential at a value of  $0.43 \text{ mmol m}^{-2} \text{ s}^{-1}$  and are comparably faster than  $r_5$ . At OER potentials each of the processes of H<sub>2</sub>O adsorption  $r_2$  and depro-

nation  $r_3$  equal the total oxygen evolution rate, i.e. the sum of both oxygen evolving steps,  $r_5$  and  $r_6$ . Since species  $*$   $\equiv$  Ir(IV) accumulates and covers 45.0% of the surface sites, even at high potentials, the H<sub>2</sub>O adsorption step is mainly limiting both OER pathways. Additionally, both oxygen evolution pathways are determined by the chemical desorption of oxygen  $r_5$  and  $r_6$ , since they converge from below and both of the reactants Ir(V) and Ir(VI) are present with quite high amount of 35.5% and 9.8% respectively.

In conclusion, the oxygen evolution in mechanism M2 is, as well as in mechanism M1, limited due to H<sub>2</sub>O adsorption and due to dual site desorption of oxygen. An accumulation of three species Ir(IV), Ir(V) and Ir(VI) is occurring and the respective subsequent reactions  $r_2$ ,  $r_3$  and  $r_6$  define the overall turnover.

### 3.5. Surface coverage of intermediate species and oxidation states

With the change in the intermediate states over the whole potential range, the mean oxidation state increases monotonously from +3 to approximately +4.7. The ascending trend matches x-ray spectroscopy results at the Ir L<sub>1</sub> and L<sub>3</sub> edge quite well [22,23]. At an OER potential of 1.6 V vs RHE, the surface species Ir(V) covers 63.4% and 35.5% of the surface for the mechanisms M1 and M2 respectively, which also is found to be present experimentally by x-ray spectroscopy measurements [23]. Ir(IV) covers 25.1% (M1) and 45.0% (M2). Interestingly, in mechanism M1 the fraction of the reduced species Ir(III) increases with high potentials, starting from its minimum of 0.01% at 1.35 V vs RHE to a coverage of 7.0% at the highest simulated potential. This species arises due to a limitation of the non-electrochemically driven adsorption reaction of H<sub>2</sub>O, as discussed above. A reported analysis of x-ray spectroscopy results matches these findings as it suggests the presence of a species with low oxidation state of  $+3.3 \pm 0.2$  [23]. In contrast, the simulation of mechanism M2 exhibits Ir(III) to decrease strictly monotonic to a value of 2.7% at OER potentials.

Thus, one may conclude the following: both mechanisms strongly differ in the adsorbed species and oxidation states, and only M1 shows some more reduced species at very high potentials. Further, M1 matches and also explains experimental findings of low oxidation states at high potentials. They are attributed to a slow water adsorption process. This suggests that the theory-derived mechanism, M1, seems to be the more likely mechanism and that accelerating OER requires better water adsorption at the catalyst.

### 3.6. Thermodynamic analysis

The presented microkinetic models use the transition state theory. This allows the calculation of thermodynamic Gibbs free reaction energies  $\Delta G$  right away from the simulation results for each reaction  $i$ :

$$\Delta G_i = -k_B T \cdot \ln \left( \frac{k_{+i}}{k_{-i}} \right) \quad (26)$$

In the experimental setup, the reversible hydrogen electrode serves as reference at pH  $\approx$  1. In consequence, all parameters are identified with respect to this special condition. To allow an appropriate comparability with other studies, we correct the energy value with respect to the generally accepted electrochemical standard conditions. This is conducted by using the following equation (for further details see B.1):

$$\Delta G_i^0 = \Delta G_i + \frac{zeRT}{F} \cdot \ln(a_{H^+}) \quad (27)$$

The results of the PCET and H<sub>2</sub>O adsorption steps are given in Fig. 7 for a) mechanism M1 and b) mechanism M2. Additionally, the standard Gibbs free energy of 1.23 eV of the overall oxygen

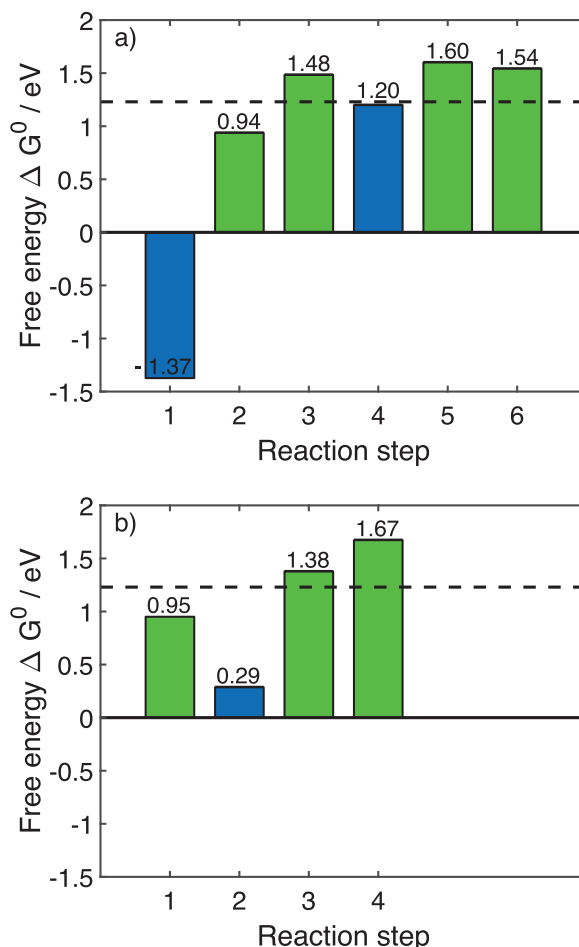


Fig. 7. Gibbs free energy for the electrochemical deprotonation reactions (green) and H<sub>2</sub>O adsorption steps (light blue) at the hydrous Ir surface under standard conditions for mechanism M1 a) and mechanism M2 b).

formation is represented by the dotted line. In M1 the overall catalytic process is limited mainly by the highest energy value, which is  $\Delta G_5^0 = 1.60$  eV. Step 6 is following without further thermodynamic limitation, since  $\Delta G_6^0 < \Delta G_5^0$ . Values gained for the electrochemical steps in mechanism M1 are qualitatively in good agreement with DFT based calculations for rutile (110) IrO<sub>2</sub> surface [52]. This suggests the hydrous iridium mechanism M1 to be related with IrO<sub>2</sub> DFT results not only from a mechanistic point of view but as well backed in the thermodynamic analysis. In M2, most unfavourable and, hence, limiting step is  $\Delta G_4^0 = 1.67$  eV. No comparable values are found in literature for M2.

Specific H<sub>2</sub>O adsorption energies are calculated to  $\Delta G_1^0 = -135.4$  kJ mol<sup>-1</sup> at Ir(III) and  $\Delta G_4^0 = 114.5$  kJ mol<sup>-1</sup> at Ir(V) for mechanism M1 and  $\Delta G_2^0 = 31.4$  kJ mol<sup>-1</sup> at Ir(IV) for mechanism M2. In comparison, calculation for (110) and (011) surfaces of rutile IrO<sub>2</sub> by ab initio molecular dynamics [68] obtain energy values of  $\Delta E_{(110)} = -211.5$  kJ mol<sup>-1</sup> and  $\Delta E_{(011)} = -145.9$  kJ mol<sup>-1</sup> for dissociative H<sub>2</sub>O adsorption. This shows for  $\Delta G_1^0$  of M1 good agreement with ab initio results.

Only taking the thermodynamics into account reveals a simplified description: the energy values are directly correlated to the potentials, above which the oxidation product of the respective reaction is energetically favorable. Thermodynamic energies are widely gained ab initio with DFT [29,52] and used to calculate CV curves with the generalised computational electrode method [69]. But since the OER is a highly dynamic reaction cycle, an analysis purely based on energy values might be oversimplified. The energy

diagram of mechanism M1 claims the formation of Ir(VI) via reaction  $r_5$  to be energetically favorable at potentials higher than 1.60 V and with this the overall OER. In contrast the results of the kinetic study suggests Ir(V), Ir(IV) and Ir(III) to be present in descending order and give evidence that oxygen is already produced. Such details need to be taken into account while analysing complex catalytic systems. Still, the energy diagrams provide an outstanding way to compare DFT based calculations with kinetic modeling.

Overall one can conclude that energy values provide an elegant way to validate microkinetic models or compare the results with other methods, such as molecular dynamics or DFT based calculations. A study approach purely based on thermodynamics simplifies the occurrence of multiple surface species and misses out important insights regarding the kinetics.

#### 4. Conclusion

Within this study, we present a systematic model-assisted approach to evaluate mechanistic reaction pathways and underlying blocking species and limiting reactions and to quantify essential microkinetic parameters based on CVs. For the first time, electrocatalytic surface adsorption and deprotonation steps prior and during the OER on hydrous Ir are analyzed based on microkinetic modelling. Two reaction mechanisms were compared: while mechanism M1 is inspired by DFT studies and mechanism M2 is proposed based on experimental insights, both are able to describe experimental CV data properly. But findings of reduced Ir(III) species at typical OER potentials and low water adsorption energy indicate clearly that only the DFT-inspired mechanism M1 is able to describe the catalytic system to the full extent. Simulations based on this mechanism give potential-dependent reaction rates for individual electrocatalytic steps. Oxygen is predominantly forming via a single site pathway  $*\text{OO} \xrightarrow{r_5} * + \text{O}_2$ . Dual site evolution although occurring at a less oxidised Ir state is negligible. Stepwise deprotonation by consecutive PCET processes reveals an increasing mean oxidation state ranging from +III at 0.45 V up to approximately +4.7 at 1.55 V. This goes along with the formation of higher oxidized intermediate states, which results in a surface covered by roughly 7% Ir(III), 25% Ir(IV) and 63% Ir(V) species at 1.55 V. During the OER, non-electrochemically driven and therefore comparably slow  $\text{H}_2\text{O}$  adsorption was found to be a crucial step in the electrocatalytic cycle. This explains experimental findings of reduced Ir(III) species at high potentials and further, water adsorption is also identified as a slow step at lower potentials. Furthermore, the Gibbs free energies and the  $\text{H}_2\text{O}$  adsorption energy were found to be equivalent to values calculated by DFT and ab initio molecular dynamic simulations. By considering these findings, mechanism M1 and the presented kinetics are able to describe all major aspects of the OER. The results suggest, that the search for catalysts and process conditions which favors or supports the adsorption of water at the surface might be a promising subject for further investigations to increase the activity of the oxygen evolution reduction.

#### Declaration of Competing Interest

The authors declare that they have no known competing financial interests or personal relationships that could have appeared to influence the work reported in this paper.

#### Credit authorship contribution statement

**Janis Geppert:** Methodology, Software, Validation, Formal analysis, Investigation, Writing - original draft, Visualization. **Fabian Kubannek:** Conceptualization, Writing - review & editing, Supervision. **Philipp Röse:** Resources, Writing - review & editing, Supervi-

sion. **Ulrike Krewer:** Conceptualization, Writing - review & editing, Supervision, Project administration, Funding acquisition.

#### Acknowledgements

We gratefully acknowledge the funding by [Deutsche Forschungsgemeinschaft \(DFG\)](#) in the framework of the priority program (SPP 2080: KR 3850/8-1).

#### Appendix A. Adsorption processes

In this section we give a brief description about the adsorption function we take into account in our model. There are several common adsorption isotherms, so the first step is to evaluate which one is describing the present electrocatalytic system best. Therefore three isotherms are selected from literature, which are based on work of Langmuir (L) [70], Temkin/Frumkin (F) [71] and van der Waals (W) [56,57]. The theory and derivation is given in literature in detail [58]. While Langmuir adsorption is restricted to the total number of adsorption sites, Frumkin adsorption takes into account interaction of adsorbed species, and van der Waals, additionally, the area occupied by each species. We show the notation of the respective isotherms given elsewhere [72]:

$$K_L \cdot a = \frac{\Gamma}{\Gamma_\infty - \Gamma} \quad (\text{A.1})$$

$$K_F \cdot a = \frac{\Gamma}{\Gamma_\infty - \Gamma} \exp\left(-\frac{2b\Gamma}{k_B T}\right) \quad (\text{A.2})$$

$$K_W \cdot a = \frac{\Gamma}{\Gamma_\infty - \Gamma} \exp\left(-\frac{2b\Gamma}{k_B T} + \frac{\Gamma}{\Gamma_\infty - \Gamma}\right) \quad (\text{A.3})$$

In these equations  $\Gamma$  is the surface concentration of the adsorbed species,  $a$  is the activity and  $K$  is the adsorption equilibrium constant and  $b$  the parameter accounting for the interaction between adsorbed species. We further simplify the term with  $g(T) = -\frac{2b}{k_B T}$ , as typically done for Frumkin or Temkin isotherms. The conversion of the equation into a form, which takes forward and backwards sorption into account, is done following the work of Laviron [59], who conducted this explicitly for Frumkin adsorption. The implementation into the kinetic equations used in the model (Eq. 15–18) was deduced from work of Vidaković [60]. This gives the adsorption functions of a forward  $f_+$  and backward  $f_-$  reaction for each respective adsorption process with the surface coverages  $\theta$  and the symmetry factor  $\beta$ :

$$f_{L,+} = 1 \quad (\text{A.4})$$

$$f_{L,-} = 1 \quad (\text{A.5})$$

$$f_{F,+} = \exp\left(\beta[g_j\theta_j^{v_{ij}} - g_j\theta_j^{v_{-ij}}]\right) \quad (\text{A.6})$$

$$f_{F,-} = \exp\left(- (1 - \beta)[g_j\theta_j^{v_{ij}} - g_j\theta_j^{v_{-ij}}]\right) \quad (\text{A.7})$$

$$f_{W,+} = \exp\left(\beta\left[g_j\theta_j^{v_{ij}} - g_j\theta_j^{v_{-ij}} + \frac{\theta_j^{v_{ij}}}{\theta_j^{v_{-ij}}} - \frac{\theta_j^{v_{-ij}}}{\theta_j^{v_{ij}}}\right]\right) \quad (\text{A.8})$$

$$f_{W,-} = \exp\left(- (1 - \beta)\left[g_j\theta_j^{v_{ij}} - g_j\theta_j^{v_{-ij}} + \frac{\theta_j^{v_{ij}}}{\theta_j^{v_{-ij}}} - \frac{\theta_j^{v_{-ij}}}{\theta_j^{v_{ij}}}\right]\right) \quad (\text{A.9})$$

**Table A.2**  
Parameter values identified with the assumption of different adsorption types.

Adsorption type	$k_+$	$k_-$ mol m <sup>-2</sup> s <sup>-1</sup>	$g_{Red}$	$g_{Ox}$	$\rho$ mol m <sup>-2</sup>	RMSE mA cm <sup>-2</sup>
Langmuir	$1.0 \cdot 10^{-9}$	$4.0 \cdot 10^9$	-	-	$1.6 \cdot 10^{-4}$	6.2
Frumkin	$5.2 \cdot 10^{-10}$	$2.0 \cdot 10^9$	4.7	4.8	$3.4 \cdot 10^{-4}$	2.0
van der Waals	$1.6 \cdot 10^{-10}$	$7.7 \cdot 10^8$	3.3	3.5	$5.0 \cdot 10^{-4}$	0.9

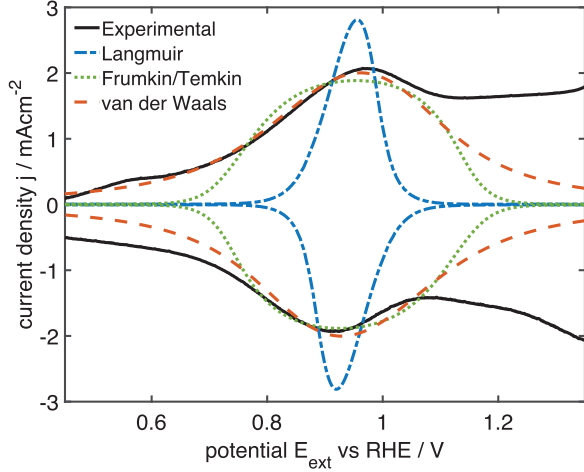


**Fig. A.8.** Simulation of Langmuir, Frumkin/Temkin and van der Waals adsorption currents of an one electron proton transfer reaction in comparison to experimental data. Kinetic parameters ( $k_+$ ,  $k_-$ ,  $g_{Red}$ ,  $g_{Ox}$  and  $\rho$  in Eq. 15 - 22) are identified in order to gain lowest RMSE values (Eq. 25) for each of the simulations separately.

To evaluate, which of the adsorption terms describe our electrocatalytic system best, we assume a single electron PCET step of a reduced to an oxidised adsorbed species ( $Red \xrightarrow{r} Ox + e^-$ ). The reaction is implemented and simulated as described in Section 2.3. The parameters given in Table A.2 are optimized onto the feature A<sub>1</sub> ( $0.6 \text{ V} < E < 1.1 \text{ V}$ ) of the experimental data shown in Fig. 3. The simulation results of modeling several adsorption isotherms in comparison with experimental data in the range  $0.4 \text{ V} < E < 1.4 \text{ V}$  are shown in Fig. A.8. Quantification of best optimization results gain RMSE values of 6.2, 2.0 and 0.9 mA cm<sup>-2</sup> for Langmuir, Frumkin/Temkin and van der Waals adsorption respectively. Langmuir fails to describe the experimentally observed broad adsorption peak, as it assumes a surface coverage independent adsorption energy, and thus leads to a narrow peak. This is in agreement with studies reporting, that the broad adsorption peak in the cyclic voltammetric data can not be explained by Langmuir adsorption [7,50]. Temkin shows a broader peak as adsorption energy depends already on coverage but it is not in line with the experimental data at potentials  $E < 0.8 \text{ V}$  and  $E > 1.1 \text{ V}$ . In best agreement is the kinetic simulation using van der Waals adsorption as it fits the data over a wide potential range with low RMSE value. With these results we conclude van der Waals, also known as Hill-de Boer, adsorption to be present at the electrode electrolyte interface. This is plausible as its theoretical derivation is based on two major assumptions [58], which both are in agreement with our electrode system: the defined areal spacing and the interaction of adsorbed species. Hence, we use van der Waals adsorption  $f = f_W$  in the model Eq. 20.

## Appendix B. Set of reaction kinetic equations and species balances

The set of model equations used to calculate reaction rates and coverage of species  $j \in \{*, \text{H}_2\text{O}, \text{OH}, \text{O}, \text{OH}_2\text{O}, \text{OOH}, \text{OO}\}$  of mechanism M1 as well as the change in coverage are given in the

following.

$$r_{+1} = k_{+1} a_{\text{H}_2\text{O}} \theta_* \cdot \exp \left( \beta \left[ g_* \theta_* - g_{\text{H}_2\text{O}} \theta_{\text{H}_2\text{O}} + \frac{\theta_*}{\theta_{\text{H}_2\text{O}}} - \frac{\theta_{\text{H}_2\text{O}}}{\theta_*} \right] \right)$$

$$r_{-1} = k_{-1} \theta_{\text{H}_2\text{O}} \cdot \exp \left( -\beta \left[ g_* \theta_* - g_{\text{H}_2\text{O}} \theta_{\text{H}_2\text{O}} + \frac{\theta_*}{\theta_{\text{H}_2\text{O}}} - \frac{\theta_{\text{H}_2\text{O}}}{\theta_*} \right] \right)$$

$$r_{+2} = k_{+2} \theta_{\text{H}_2\text{O}} \cdot \exp \left( \beta \left[ g_{\text{H}_2\text{O}} \theta_{\text{H}_2\text{O}} - g_{\text{OH}} \theta_{\text{OH}} + \frac{\theta_{\text{H}_2\text{O}}}{\theta_{\text{OH}}} - \frac{\theta_{\text{OH}}}{\theta_{\text{H}_2\text{O}}} \right] \right) \cdot \exp \left( \frac{\beta F}{RT} E \right)$$

$$r_{-2} = k_{-2} a_{\text{H}^+} \theta_{\text{OH}} \cdot \exp \left( -\beta \left[ g_{\text{H}_2\text{O}} \theta_{\text{H}_2\text{O}} - g_{\text{OH}} \theta_{\text{OH}} + \frac{\theta_{\text{H}_2\text{O}}}{\theta_{\text{OH}}} - \frac{\theta_{\text{OH}}}{\theta_{\text{H}_2\text{O}}} \right] \right) \cdot \exp \left( \frac{-\beta F}{RT} E \right)$$

$$r_{+3} = k_{+3} \theta_{\text{OH}} \cdot \exp \left( \beta \left[ g_{\text{OH}} \theta_{\text{OH}} - g_{\text{O}} \theta_{\text{O}} + \frac{\theta_{\text{OH}}}{\theta_{\text{O}}} - \frac{\theta_{\text{O}}}{\theta_{\text{OH}}} \right] \right) \cdot \exp \left( \frac{\beta F}{RT} E \right)$$

$$r_{-3} = k_{-3} a_{\text{H}^+} \theta_{\text{O}} \cdot \exp \left( -\beta \left[ g_{\text{SOH}} \theta_{\text{SOH}} - g_{\text{SO}} \theta_{\text{SO}} + \frac{\theta_{\text{OH}}}{\theta_{\text{O}}} - \frac{\theta_{\text{O}}}{\theta_{\text{OH}}} \right] \right) \cdot \exp \left( \frac{-\beta F}{RT} E \right)$$

$$r_{+4} = k_{+4} a_{\text{H}_2\text{O}} \theta_{\text{O}} \cdot \exp \left( \beta \left[ g_{\text{O}} \theta_{\text{O}} - g_{\text{OH}_2\text{O}} \theta_{\text{OH}_2\text{O}} + \frac{\theta_{\text{O}}}{\theta_{\text{OH}_2\text{O}}} - \frac{\theta_{\text{OH}_2\text{O}}}{\theta_{\text{O}}} \right] \right)$$

$$r_{-4} = k_{-4} \theta_{\text{OH}_2\text{O}} \cdot \exp \left( -\beta \left[ g_{\text{O}} \theta_{\text{O}} - g_{\text{OH}_2\text{O}} \theta_{\text{OH}_2\text{O}} + \frac{\theta_{\text{O}}}{\theta_{\text{OH}_2\text{O}}} - \frac{\theta_{\text{OH}_2\text{O}}}{\theta_{\text{O}}} \right] \right)$$

$$r_{+5} = k_{+5} \theta_{\text{OH}_2\text{O}} \cdot \exp \left( \beta \left[ g_{\text{OH}_2\text{O}} \theta_{\text{OH}_2\text{O}} - g_{\text{OOH}} \theta_{\text{OOH}} + \frac{\theta_{\text{OH}_2\text{O}}}{\theta_{\text{OOH}}} - \frac{\theta_{\text{OOH}}}{\theta_{\text{OH}_2\text{O}}} \right] \right) \cdot \exp \left( \frac{\beta F}{RT} E \right)$$

$$r_{-5} = k_{-5} a_{\text{H}^+} \theta_{\text{OOH}} \cdot \exp \left( -\beta \left[ g_{\text{OH}_2\text{O}} \theta_{\text{OH}_2\text{O}} - g_{\text{OOH}} \theta_{\text{OOH}} + \frac{\theta_{\text{OH}_2\text{O}}}{\theta_{\text{OOH}}} - \frac{\theta_{\text{OOH}}}{\theta_{\text{OH}_2\text{O}}} \right] \right) \cdot \exp \left( \frac{-\beta F}{RT} E \right)$$

$$r_{+6} = k_{+6} \theta_{\text{OOH}} \cdot \exp \left( \beta \left[ g_{\text{OOH}} \theta_{\text{OOH}} - g_{\text{OO}} \theta_{\text{OO}} + \frac{\theta_{\text{OOH}}}{\theta_{\text{OO}}} - \frac{\theta_{\text{OO}}}{\theta_{\text{OOH}}} \right] \right) \cdot \exp \left( \frac{\beta F}{RT} E \right)$$

$$r_{-6} = k_{-6} a_{\text{H}^+} \theta_{\text{OO}} \cdot \exp \left( -\beta \left[ g_{\text{OOH}} \theta_{\text{OOH}} - g_{\text{OO}} \theta_{\text{OO}} + \frac{\theta_{\text{OOH}}}{\theta_{\text{OO}}} - \frac{\theta_{\text{OO}}}{\theta_{\text{OOH}}} \right] \right) \cdot \exp \left( \frac{-\beta F}{RT} E \right)$$

$$r_{+7} = k_{+7} \theta_{\text{O}}^2 \cdot \exp \left( \beta \left[ g_{\text{O}} \theta_{\text{O}} - g_* \theta_* + \frac{\theta_{\text{O}}}{\theta_*} - \frac{\theta_*}{\theta_{\text{O}}} \right] \right)$$

$$r_{+8} = k_{+8} \theta_{\text{OO}} \cdot \exp \left( \beta \left[ g_{\text{OO}} \theta_{\text{OO}} - g_* \theta_* + \frac{\theta_{\text{OO}}}{\theta_*} - \frac{\theta_*}{\theta_{\text{OO}}} \right] \right)$$

$$\frac{d\theta_*}{dt} = \frac{1}{\rho} (-r_{+1} + r_{-1} + r_{+7} + r_{+8})$$

$$\frac{d\theta_{\text{H}_2\text{O}}}{dt} = \frac{1}{\rho} (r_{+1} - r_{-1} - r_{+2} + r_{-2})$$

$$\frac{d\theta_{OH}}{dt} = \frac{1}{\rho} (r_{+2} - r_{-2} - r_{+3} + r_{-3})$$

$$\frac{d\theta_O}{dt} = \frac{1}{\rho} (r_{+3} - r_{-3} - r_{+4} + r_{-4} - r_{+7})$$

$$\frac{d\theta_{OH_2O}}{dt} = \frac{1}{\rho} (r_{+4} - r_{-4} - r_{+5} + r_{-5})$$

$$\frac{d\theta_{OOH}}{dt} = \frac{1}{\rho} (r_{+5} - r_{-5} - r_{+6} + r_{-6})$$

$$\frac{d\theta_{OO}}{dt} = \frac{1}{\rho} (r_{+6} - r_{-6} - r_{+8})$$

The set of model equations used to calculate reaction rates and coverage of species  $j \in \{H, *, H_2O, OH, O\}$  of mechanism M2 as well as the change in coverage are given as follows.

$$r_{+1} = k_{+1}\theta_H \cdot \exp\left(\beta\left[g_H\theta_H - g_*\theta_* + \frac{\theta_H}{\theta_*} - \frac{\theta_*}{\theta_H}\right]\right) \cdot \exp\left(\frac{\beta F}{RT}E\right)$$

$$r_{-1} = k_{-1}a_{H^+}\theta_* \cdot \exp\left(-\beta\left[g_H\theta_H - g_*\theta_* + \frac{\theta_H}{\theta_*} - \frac{\theta_*}{\theta_H}\right]\right) \cdot \exp\left(\frac{-\beta F}{RT}E\right)$$

$$r_{+2} = k_{+2}a_{H_2O}\theta_* \cdot \exp\left(\beta\left[g_*\theta_* - g_{H_2O}\theta_{H_2O} + \frac{\theta_*}{\theta_{H_2O}} - \frac{\theta_{H_2O}}{\theta_*}\right]\right)$$

$$r_{-2} = k_{-2}\theta_{H_2O} \cdot \exp\left(-\beta\left[g_*\theta_* - g_{H_2O}\theta_{H_2O} + \frac{\theta_*}{\theta_{H_2O}} - \frac{\theta_{H_2O}}{\theta_*}\right]\right)$$

$$r_{+3} = k_{+3}\theta_{H_2O} \cdot \exp\left(\beta\left[g_{H_2O}\theta_{H_2O} - g_{OH}\theta_{OH} + \frac{\theta_{H_2O}}{\theta_{OH}} - \frac{\theta_{OH}}{\theta_{H_2O}}\right]\right) \cdot \exp\left(\frac{\beta F}{RT}E\right)$$

$$r_{-3} = k_{-3}a_{H^+}\theta_{OH} \cdot \exp\left(-\beta\left[g_{H_2O}\theta_{H_2O} - g_{OH}\theta_{OH} + \frac{\theta_{H_2O}}{\theta_{OH}} - \frac{\theta_{OH}}{\theta_{H_2O}}\right]\right) \cdot \exp\left(\frac{-\beta F}{RT}E\right)$$

$$r_{+4} = k_{+4}\theta_{OH} \cdot \exp\left(\beta\left[g_{OH}\theta_{OH} - g_O\theta_O + \frac{\theta_{OH}}{\theta_O} - \frac{\theta_O}{\theta_{OH}}\right]\right) \cdot \exp\left(\frac{\beta F}{RT}E\right)$$

$$r_{-4} = k_{-4}a_{H^+}\theta_O \cdot \exp\left(-\beta\left[g_{OH}\theta_{OH} - g_O\theta_O + \frac{\theta_{OH}}{\theta_O} - \frac{\theta_O}{\theta_{OH}}\right]\right) \cdot \exp\left(\frac{-\beta F}{RT}E\right)$$

$$r_{+5} = k_{+5}\theta_O^2 \cdot \exp\left(\beta\left[g_O\theta_O - g_*\theta_* + \frac{\theta_O}{\theta_*} - \frac{\theta_*}{\theta_O}\right]\right)$$

$$r_{+6} = k_{+6}\theta_{OH}^2 \cdot \exp\left(\beta\left[g_{OH}\theta_{OH} - g_H\theta_H + \frac{\theta_{OH}}{\theta_H} - \frac{\theta_H}{\theta_{OH}}\right]\right)$$

$$\frac{d\theta_H}{dt} = \frac{1}{\rho} (-r_{+1} + r_{-1} + r_{+6})$$

$$\frac{d\theta_*}{dt} = \frac{1}{\rho} (r_{+1} - r_{-1} - r_{+2} + r_{-2} + r_{+5})$$

$$\frac{d\theta_{H_2O}}{dt} = \frac{1}{\rho} (r_{+2} - r_{-2} - r_{+3} + r_{-3})$$

$$\frac{d\theta_{OH}}{dt} = \frac{1}{\rho} (r_{+3} - r_{-3} - r_{+4} + r_{-4} - r_{+6})$$

$$\frac{d\theta_O}{dt} = \frac{1}{\rho} (r_{+4} - r_{-4} - r_{+5})$$

### B1. Consistency with nernst potential

In this section we demonstrate that the microkinetic formulations in Eqs. 15 - 18 are consistent with the basics of electrochemical theory. This is done by assuming equilibrium of the electrochemical forward (Eq. 16) and backward (Eq. 18) reaction rates  $r_{E,+i} = r_{E,-i}$  and compare the outcome to the Nernst potential.

$$\exp\left(\frac{zF}{RT} \cdot E\right) = \frac{k_{-i}}{k_{+i}} \cdot \frac{\prod_{j \in S} (a_j^{v_{-ij}} \cdot \theta_j^{v_{-ij}} \cdot f_-)}{\prod_{j \in S} (a_j^{v_{+ij}} \cdot \theta_j^{v_{+ij}} \cdot f_+)} \quad (B.1)$$

The kinetic equilibrium constant  $K_i = k_{+i}/k_{-i}$  is related to the Gibbs free energy of reaction  $K_i = \exp[-\Delta G_i/(k_B T)]$ .

$$E = \frac{\Delta G_i}{ze} + \frac{RT}{zF} \ln\left(\prod_{j \in S} \left[\frac{a_j^{v_{-ij}} \cdot \theta_j^{v_{-ij}} \cdot f_-}{a_j^{v_{+ij}} \cdot \theta_j^{v_{+ij}} \cdot f_+}\right]\right) \quad (B.2)$$

As stated in the main paper, potential  $E$  is given versus the reversible hydrogen electrode RHE. Conversion to standard conditions with respect to the standard hydrogen electrode (SHE) is done by taking changes with pH into account  $E_{SHE} + E^{00} = E + E^{00} + RT/F \cdot \ln(a_{H^+})$  with the standard reference potential  $E^{00} = 0$  V.

$$E_{SHE} = \frac{RT}{F} \cdot \ln(a_{H^+}) + \frac{\Delta G_i}{ze} + \frac{RT}{zF} \ln\left(\prod_{j \in S} \left[\frac{a_j^{v_{-ij}} \cdot \theta_j^{v_{-ij}} \cdot f_-}{a_j^{v_{+ij}} \cdot \theta_j^{v_{+ij}} \cdot f_+}\right]\right) \quad (B.3)$$

$$E_{SHE} = \frac{\Delta G_i^0}{ze} + \frac{RT}{zF} \ln\left(\prod_{j \in S} \left[\frac{a_j^{v_{-ij}} \cdot \theta_j^{v_{-ij}} \cdot f_-}{a_j^{v_{+ij}} \cdot \theta_j^{v_{+ij}} \cdot f_+}\right]\right) \quad (B.4)$$

In the last step the Gibbs free energy of the reaction is also corrected with respect to the pH value to gain the standard Gibbs free energy  $\Delta G_i^0 = \Delta G_i + zeRT/F \cdot \ln(a_{H^+})$ . The resulting Eq. B.4 can directly identified with the Nernst equation, by excluding the function of the adsorption  $f$ , which is not taken into account in the Nernst theory. This calculation shows the consistency of the model equation with standard conditions and the fundamental Nernst equation.

### References

- [1] K.F. Kalz, R. Kraehnert, M. Dvoyashkin, R. Dittmeyer, R. Gläser, U. Krewer, K. Reuter, J.D. Grunwaldt, Future challenges in heterogeneous catalysis: understanding catalysts under dynamic reaction conditions, *ChemCatChem* 9 (2017) 17.
- [2] W. Böld, M. Breiter, Untersuchung des anodischen aufbaus und der kathodischen reduktion der sauerstoffbelegung am rhodium und iridium, *Electrochim. Acta* 5 (1961) 169.
- [3] D.A.J. Rand, R. Woods, P. Melbourne, Cyclic voltammetric studies on iridium electrodes in sulphuric acid solutions, *J. Electroanal. Chem.* 55 (1974) 375.
- [4] M.A. Petit, V. Plichon, Anodic electrodeposition of iridium oxide films, *J. Electroanal. Chem.* 444 (1998) 247.
- [5] S. Cherevko, S. Geiger, O. Kasian, A. Mingers, K.J. Mayrhofer, Oxygen evolution activity and stability of iridium in acidic media. Part 2. - Electrochemically grown hydrous iridium oxide, *J. Electroanal. Chem.* 774 (2016) 102.
- [6] S. Cherevko, A.R. Zeradjanin, A.A. Topalov, N. Kulyk, I. Katsounaros, K.J. Mayrhofer, Dissolution of noble metals during oxygen evolution in acidic media, *ChemCatChem* 6 (2014) 2219.
- [7] S. Cherevko, S. Geiger, O. Kasian, N. Kulyk, J.P. Grote, A. Sazan, B.R. Shrestha, S. Merzlikin, B. Breitbach, A. Ludwig, K.J. Mayrhofer, Oxygen and hydrogen evolution reactions on Ru, RuO<sub>2</sub>, Ir, and IrO<sub>2</sub> thin film electrodes in acidic and alkaline electrolytes: a comparative study on activity and stability, *Catal. Today* 262 (2016) 170.

- [8] O. Kasian, S. Geiger, T. Li, J.P. Grote, K. Schweinar, S. Zhang, C. Scheu, D. Raabe, S. Cherevko, B. Gault, K.J. Mayrhofer, Degradation of iridium oxides via oxygen evolution from the lattice: correlating atomic scale structure with reaction mechanisms, *Energy Environ. Sci.* 12 (2019) 3548.
- [9] J.O. Bockris, Kinetics of activation controlled consecutive electrochemical reactions: anodic evolution of oxygen, *J. Chem. Phys.* 24 (1956) 817.
- [10] B.E. Conway, J. Mozota, Behaviour processes at oxidized iridium, *Electrochim. Acta* 28 (1983) 9.
- [11] J. Mozota, B.E. Conway, Surface and bulk processes at oxidized iridium stage and transition to reversible oxide film behaviour, *Electrochim. Acta* 28 (1983) 1.
- [12] L.D. Burke, J.K. Mulcahy, D.P. Whelan, Preparation of an oxidized iridium electrode and the variation of its potential with pH, *J. Electroanal. Chem.* 163 (1984) 117.
- [13] P.G. Pickup, V.I. Birss, The kinetics of charging and discharging of iridium oxide films in aqueous and non-aqueous media, *J. Electroanal. Chem.* 240 (1988) 185.
- [14] S. Gottesfeld, S. Srinivasan, Electrochemical and optical studies of thick oxide layers on iridium and their electrocatalytic activities for the oxygen evolution reaction, *J. Electroanal. Chem.* 86 (1978) 89.
- [15] D.N. Buckley, L.D. Burke, The oxygen electrode. Part 5.—Enhancement of charge capacity of an iridium surface in the anodic region, *J. Chem. Soc., Faraday Trans. 1* 71 (1975) 1447.
- [16] R. Kötz, H. Neff, S. Stucki, Anodic iridium oxide films: XPS-studies of oxidation state changes and O<sub>2</sub>-evolution, *J. Electrochem. Soc.* 131 (1984) 72.
- [17] D. Michell, D.A.J. Rand, R. Woods, Analysis of the anodic oxygen layer on iridium by X-ray emission, electron diffraction and electron microscopy, *J. Electroanal. Chem.* 84 (1977) 117.
- [18] Y. Mo, I.C. Stefan, W.B. Cai, J. Dong, P. Carey, D.A. Scherson, In situ iridium LIII-edge X-ray absorption and surface enhanced Raman spectroscopy of electrodeposited iridium oxide films in aqueous electrolytes, *J. Phys. Chem. B* 106 (2002) 3681.
- [19] S. Geiger, O. Kasian, B.R. Shrestha, A.M. Mingers, K.J.J. Mayrhofer, S. Cherevko, Activity and stability of electrochemically and thermally treated iridium for the oxygen evolution reaction, *J. Electrochem. Soc.* 163 (2016) F3132.
- [20] G.C. da Silva, N. Perini, E.A. Ticianelli, Effect of temperature on the activities and stabilities of hydrothermally prepared IrO<sub>x</sub> nanocatalyst layers for the oxygen evolution reaction, *Appl. Catal. B-Environ.* 218 (2017) 287.
- [21] V. Pfeifer, T.E. Jones, J.J. Velasco Vélez, C. Massué, R. Arrigo, D. Teschner, F. Girgsdies, M. Scherzer, M.T. Greiner, J. Allan, M. Hashagen, G. Weinberg, S. Piccinin, M. Hävecker, A. Knop-Gericke, R. Schlögl, The electronic structure of iridium and its oxides, *Surf. Interface Anal.* 48 (2016) 261.
- [22] M. Hüppauff, Valency and structure of iridium in anodic iridium oxide films, *J. Electrochem. Soc.* 140 (2006) 598.
- [23] A. Minguzzi, O. Lugaresi, E. Achilli, C. Locatelli, A. Vertova, P. Ghigna, S. Rondinini, Observing the oxidation state turnover in heterogeneous iridium-based water oxidation catalysts, *Chem. Sci.* 5 (2014) 3591.
- [24] A.R. Hillman, M.A. Skopek, S.J. Gurman, X-ray spectroscopy of electrochemically deposited iridium oxide films: Detection of multiple sites through structural disorder, *Phys. Chem. Chem. Phys.* 13 (2011) 5252.
- [25] V.A. Saveleva, L. Wang, D. Teschner, T. Jones, A.S. Gago, K.A. Friedrich, S. Zafeiratou, R. Schlögl, E.R. Savinova, Operando evidence for a universal oxygen evolution mechanism on thermal and electrochemical iridium oxides, *J. Phys. Chem. Lett.* 9 (2018) 3154.
- [26] S. Trasatti, Electrocatalysis in the anodic evolution of oxygen and chlorine, *Electrochim. Acta* 29 (1984) 1503.
- [27] A. Damjanovic, A. Dey, J.O. Bockris, Electrode kinetics of oxygen evolution and dissolution on Rh, Ir, and Pt-Rh alloy electrodes, *J. Electrochem. Soc.* 113 (1966) 739.
- [28] J. Rossmeisl, A. Logadottir, J.K. Nørskov, Electrolysis of water on (oxidized) metal surfaces, *Chem. Phys.* 319 (2005) 178.
- [29] J. Rossmeisl, Z.-W. Qu, H. Zhu, G.-J. Kroes, J. Nørskov, Electrolysis of water on oxide surfaces, *J. Electroanal. Chem.* 607 (2007) 83.
- [30] Y. Ping, R.J. Nielsen, W.A. Goddard, The reaction mechanism with free energy barriers at constant potentials for the oxygen evolution reaction at the IrO<sub>2</sub> (110) surface, *J. Am. Chem. Soc.* 139 (2017) 149.
- [31] J.M. Hu, J.Q. Zhang, C.N. Cao, Oxygen evolution reaction on IrO<sub>2</sub>-based DSA-type electrodes: kinetics analysis of Tafel lines and EIS, *Int. J. Hydrogen Energy* 29 (2004) 791.
- [32] A.P. Dam, G. Papakonstantinou, K. Sundmacher, On the role of microkinetic network structure in the interplay between oxygen evolution reaction and catalyst dissolution, *Sci. Rep.* 10 (2020) 14140.
- [33] L.F.L. Oliveira, S. Laref, E. Mayousse, C. Jallut, A.a. Franco, A multiscale physical model for the transient analysis of PEM water electrolyzer anodes, *Phys. Chem. Chem. Phys.* 14 (2012) 1021.
- [34] T. Shinagawa, A.T. Garcia-Esparza, K. Takanabe, Insight on Tafel slopes from a microkinetic analysis of aqueous electrocatalysis for energy conversion, *Sci. Rep.* 5 (2015) 1.
- [35] F.J. Vidal-Iglesias, J. Solla-Gullón, V. Montiel, A. Aldaz, An easy method for calculating kinetic parameters of electrochemical mechanisms: Temkin's formalism, *Electrocatalysis* 6 (2015) 148.
- [36] A.T. Marshall, L. Vaisson-Béthune, Avoid the quasi-equilibrium assumption when evaluating the electrocatalytic oxygen evolution reaction mechanism by Tafel slope analysis, *Electrochem. Commun.* 61 (2015) 23.
- [37] A.T. Marshall, A. Herritsch, Understanding the hydrogen and oxygen evolution reactions through microkinetic models, *ECS Trans.* 85 (2018) 121.
- [38] P. Schön, U. Krewer, Revealing the complex sulfur reduction mechanism using cyclic voltammetry simulation, *Electrochim. Acta* 373 (2021) 137523.
- [39] T. Haisch, F. Kubannek, L. Nikitina, I. Nikitin, S. Pott, T. Clees, U. Krewer, The origin of the hysteresis in cyclic voltammetric response of alkaline methanol electrooxidation, *Phys. Chem. Chem. Phys.* 22 (2020) 16648.
- [40] T. Clees, I. Nikitin, L. Nikitina, S. Pott, U. Krewer, T. Haisch, Parameter identification in cyclic voltammetry of alkaline methanol oxidation, in: *Proceedings of 8th International Conference on Simulation and Modeling Methodologies, Technologies and Applications - Volume 1: SIMULTECH*, SciTePress, 2018, p. 279.
- [41] F. Kubannek, U. Krewer, A cyclone flow cell for quantitative analysis of kinetics at porous electrodes by differential electrochemical mass spectrometry, *Electrochim. Acta* 210 (2016) 862.
- [42] M. Röhe, F. Kubannek, U. Krewer, Processes and their limitations in oxygen depolarized cathodes: a dynamic model-based analysis, *ChemSusChem* 12 (2019) 2373.
- [43] M. Heinrich, N. Wolff, N. Harting, V. Laue, F. Röder, S. Seitz, U. Krewer, Physico-chemical modeling of a lithium-ion battery: an ageing study with electrochemical impedance spectroscopy, *Batteries Supercaps* 2 (2019) 530.
- [44] U. Krewer, M. Christov, T. Vidaković, K. Sundmacher, Impedance spectroscopic analysis of the electrochemical methanol oxidation kinetics, *J. Electroanal. Chem.* 589 (2006) 148.
- [45] U. Krewer, T. Vidaković-Koch, L. Rihko-Struckmann, Electrochemical oxidation of carbon-containing fuels and their dynamics in low-temperature fuel cells, *ChemPhysChem* 12 (2011) 2518.
- [46] N. Wolff, N. Harting, F. Röder, M. Heinrich, U. Krewer, Understanding nonlinearity in electrochemical systems, *Eur. Phys. J. Special Top.* 227 (2019) 2617.
- [47] T.R. Vidaković-Koch, V.V. Panić, M. Andrić, M. Petkovska, K. Sundmacher, Non-linear frequency response analysis of the ferrocyanide oxidation kinetics, part i. a theoretical analysis, *J. Phys. Chem. C* 115 (2011) 17341.
- [48] J.M. Otten, W. Visscher, The anodic behaviour of iridium. I. The effect of potential cycling, *J. Electroanal. Chem.* 55 (1974) 1.
- [49] V. Birss, Electron microscopy study of formation of thick oxide films on ir and ru electrodes, *J. Electrochem. Soc.* 131 (1984) 1502.
- [50] P. Steegstra, M. Busch, I. Panas, E. Ahlberg, Revisiting the redox properties of hydrous iridium oxide films in the context of oxygen evolution, *J. Phys. Chem. C* 117 (2013) 20975.
- [51] O. Kasian, J.P. Grote, S. Geiger, S. Cherevko, K.J. Mayrhofer, The common intermediates of oxygen evolution and dissolution reactions during water electrolysis on iridium, *Angew. Chem. Int. Ed.* 57 (2018) 2488.
- [52] K. Klyukin, A. Zagalskaya, V. Alexandrov, Ab initio thermodynamics of iridium surface oxidation and oxygen evolution reaction, *J. Phys. Chem. C* 122 (2018) 29350.
- [53] R.R. Rao, M.J. Kolb, N.B. Halck, A.F. Pedersen, A. Mehta, H. You, K.A. Stoerzinger, Z. Feng, H.A. Hansen, H. Zhou, L. Giordano, J. Rossmeisl, T. Vegge, I. Chorkendorff, I.E.L. Stephens, Y. Shao-Horn, Towards identifying the active sites on RuO<sub>2</sub>(110) in catalyzing oxygen evolution, *Energy Environ. Sci.* 10 (2017) 2626.
- [54] H.A. Hansen, V. Viswanathan, J.K. Nørskov, Unifying kinetic and thermodynamic analysis of 2 e<sup>-</sup> and 4 e<sup>-</sup> reduction of oxygen on metal surfaces, *J. Phys. Chem. C* 118 (2014) 6706.
- [55] W.G. Bessler, S. Gewies, M. Vogler, A new framework for physically based modeling of solid oxide fuel cells, *Electrochim. Acta* 53 (2007) 1782.
- [56] E. Hückel, General discussion, *Trans. Faraday Soc.* 28 (1932) 442.
- [57] H.M. Cassel, Cluster formation and phase transitions in the adsorbed state, *J. Phys. Chem.* 48 (4) (1944) 195.
- [58] J.H. de Boer, *The Dynamical Character of Adsorption*, Oxford University Press, 1953.
- [59] E. Laviron, The use of linear potential sweep voltammetry and of a.c. voltammetry for the study of the surface electrochemical reaction of strongly adsorbed systems and of redox modified electrodes, *J. Electroanal. Chem.* 100 (1979) 263.
- [60] T. Vidaković, M. Christov, K. Sundmacher, A method for rough estimation of the catalyst surface area in a fuel cell, *J. Appl. Electrochem.* 39 (2009) 213.
- [61] K. Das, Single ion activities in aqueous sulfuric acid solutions: A new extra-thermodynamic assumption, *J. Solut. Chem.* 17 (1988) 327.
- [62] E.B. Robertson, H.B. Dunford, The state of the proton in aqueous sulfuric acid, *J. Am. Chem. Soc.* 86 (1964) 5080.
- [63] P.G. Pickup, V.I. Birss, A model for anodic hydrous oxide growth at iridium, *J. Electroanal. Chem.* 220 (1987) 83.
- [64] J.D.E. McIntyre, S. Basu, W.F. Peck, W.L. Brown, W.M. Augustyniak, Cation insertion reactions of electrochromic tungsten and iridium oxide films, *Phys. Rev. B* 25 (2002) 7242.
- [65] L.D. Burke, E.J. O'Sullivan, Oxygen gas evolution on hydrous oxides - an example of three-dimensional electrocatalysis? *J. Electroanal. Chem.* 117 (1981) 155.
- [66] K.A. Stoerzinger, L. Qiao, M.D. Biegalski, Y. Shao-Horn, Orientation-dependent oxygen evolution activities of rutile IrO<sub>2</sub> and RuO<sub>2</sub>, *J. Phys. Chem. Lett.* 5 (2014) 1636.
- [67] S. Gottesfeld, Electrochromism in anodic iridium oxide films, *J. Electrochem. Soc.* 126 (1979) 742.
- [68] D. González, J. Heras-Domingo, S. Pantaleone, A. Rimola, L. Rodríguez-Santiago, X. Solans-Monfort, M. Sodupe, Water adsorption on MO<sub>2</sub> (M = Ti, Ru, and Ir) surfaces. Importance of octahedral distortion and cooperative effects, *ACS Omega* 4 (2019) 2989.

- [69] A. Bagger, R.M. Arán-Ais, J. Halldin Stenlid, E. Campos dos Santos, L. Arnarson, K. Degn Jensen, M. Escudero-Escribano, B. Roldan Cuenya, J. Rossmeisl, Ab initio cyclic voltammetry on Cu(111), Cu(100) and Cu(110) in acidic, neutral and alkaline solutions, *ChemPhysChem* 20 (2019) 3096.
- [70] I. Langmuir, The adsorption of gases on plane surfaces of glass, mica and platinum, *J. Am. Chem. Soc.* 40 (9) (1918) 1361.
- [71] A. Frumkin, Die kapillarkurve der höheren fettsäuren und die Zustandsgleichung der oberflächenschicht, *Z. Phys. Chem.* 116U (1925) 466.
- [72] P.A. Kralchevsky, K.D. Danov, G. Broze, A. Mehreteab, Thermodynamics of ionic surfactant adsorption with account for the counterion binding: effect of salts of various valency, *Langmuir* 15 (1999) 2351.